Journal of the Meteorological Society of Japan

EARLY ONLINE RELEASE

The DOI for this manuscript is

DOI:10.2151/jmsj.2022-025

J-STAGE Advance published date: February 3rd, 2022

The final manuscript after publication will replace the preliminary version at the above DOI once it is available.

Qualifying Contributions of Teleconnection Patterns to Extremely Hot Summers in Japan

Atsushi MOGI[1]

and

Masahiro WATANABE[1]

1: Atmosphere and Ocean Research Institute, The University of Tokyo

Journal of the Meteorological Society of Japan

Submitted on 20 April, 2021

Revised on 14 September, 2021

Revised on 1 November, 2021

Revised on 1 December, 2021

Corresponding author:

A. Mogi, Atmosphere and Ocean Research Institute, The University of Tokyo

5-1-5 Kashiwanoha, Kashiwa, Chiba 277-8568, Japan

E-mail: at_mogi@aori.u-tokyo.ac.jp

Abstract

Extremely hot days in Japan are known to persist for a week or more, and they are measured by the temperature anomaly at 850 hPa averaged over Japan derived from the JRA-55 reanalysis data, denoted as T850JP. Severe high-temperature anomalies are often accompanied by multiple teleconnection patterns that affect the weather in Japan, but their relative contribution to individual heat wave events has not yet been quantified. In this study, we examined the effects of three major teleconnection patterns, namely, the Pacific-Japan (PJ), circumglobal teleconnection (CGT), and Siberian patterns, on T850JP in July and August from 1958–2019 using daily low-pass filtered anomalies with 8 days cutoff time-scale derived from the reanalysis.

A linear regression analysis demonstrated that T850JP tended to show a large positive anomaly one or two days after the peak of these patterns. Based on this relationship, we reconstructed a daily T850JP time series using a multivariate statistical model wherein the parameters were estimated using regression analyses between T850JP and indices of the three teleconnection patterns. The reconstructed T850JP showed that the three teleconnection patterns together accounted for 50% of the total variance of T850JP for extremely hot summers, to which each of the three teleconnection patterns were found to have a similar degree of contribution. The statistical model reproduces the interannual variability along with the long-term T850JP trend. The PJ pattern has the largest effect on the interannual variability of T850JP, probably due to the PJ teleconnection occurring over a longer timescale compared with the other two patterns. The reconstructed T850JP also displays a warming trend associated with an increasing trend in the CGT index, which may be a factor, along with the

direct thermodynamic effects due to global warming, to explain the long-term increase in the heat wave frequency in Japan.

Keywords

Japan summer temperature, Pacific-Japan pattern, circumglobal teleconnection, Siberian pattern, statistical model

1. Introduction

Heat waves are abnormally and uncomfortably hot weather that lasts from several days to several weeks, and their practical definitions vary by region or country. In Japan, extremely hot days, or *moushobi* in Japanese, are often used as a measure of heat waves, which are defined by daily maximum temperatures exceeding 35 °C. Their occurrence has increased over the last six decades in Japan (Fig. 1a). They occur irregularly in a nonlinear weather system, but global warming has been suggested to contribute to the occurrence of at least some of the recent events (Imada et al. 2019). In 1994, nearly 600 people passed away from heat stroke associated with the most severe heat wave since 1968 in Japan (Nakai et al. 1997). According to statistics from the Ministry of Health, Labor and Welfare, Japan, mortality increased during heat waves in 2010, 2013, and 2018. Fujibe (2013) reported that heat mortality changes by 40–60% per 1 °C warming in the summer mean state, and further examined the heat stroke mortality and temperature conditions in Japan in the following studies (Fujibe et al. 2018a, 2018b). As summer heat waves increase the risk to human health, understanding their mechanism and predictability is vital for both meteorology and society.

In summer over East Asia, extremely hot temperatures are reported to be associated with large-scale atmospheric circulation. Park and Schubert (1997) analyzed heat waves of 1994 over East Asian regions and found that persistent stationary waves extending from northern Europe resulted in an anomalous northward shift of the jet over East Asia and hence triggered heat waves. Guan and Yamagata (2003) pointed out that the Indian Ocean Dipole was one of the possible causes of the 1994 event. Yeo *et al.* (2019) examined heat waves over Korea during 1979–2017 and concluded that most of the heat waves in Korea can be classified into two categories: those associated with wave activities through Eurasia and those associated with convective activity in the northwest Pacific.

Previous studies have shown that three teleconnection patterns are significantly related to summer temperature variability in Japan (Ding and Wang 2005; Kosaka and Nakamura 2008; Park and Ahn 2014). These are the Pacific-Japan (PJ) pattern (Nitta 1987), circumglobal teleconnection (CGT) pattern (Hoskins and Ambrizzi 1993), and the blocking high over Siberia (Nakamura and Fukamachi 2004); they are dominant over East Asia and more persistent than synoptic weather disturbances.

The PJ pattern is a dominant dynamical mode of circulation variability over the subtropical western Pacific in summer and is known to be excited by convection anomalies over the Philippine Sea region. When the PJ pattern is positive, a high-pressure anomaly covers Japan in the lower troposphere due to a stationary Rossby wave train propagating northeastward from the Philippine Sea region; therefore, the temperature tends to be high in Japan. The CGT pattern, or the Silk Road pattern (Enomoto et al. 2003), refers to a stationary Rossby wave trapped by the Asian subtropical jet in the upper troposphere. It influences the intensity and location of the South Asian high, as the CGT pattern causes jet meandering. When the downstream of the CGT pattern reaches Japan, the temperature is affected by low-level circulation changes. The blocking high over Siberia also impacts the temperature over Japan, wherein its occurrence accompanies a cold advection to the east, which decreases the temperature around Japan. The blocking high in summer is associated with the meandering of the polar jet (Nakamura and Fukamachi 2004; Arai and Kimoto 2008); therefore, it is hereafter referred to as the Siberian pattern.

The above three patterns are suggested to predominantly influence the anomalous summer climate in Japan (Wakabayashi and Kawamura 2004) and are therefore monitored to diagnose long-range weather over Japan in summer. For instance, the Japan Meteorological Agency (JMA) concluded that the PJ and CGT patterns were the dominant causes of heat waves in Japan in 2018 (JMA 2018). However, the pattern responsible for individual hot summer events in the past is not yet clear, as the atmospheric circulation pattern actually differs in each event; therefore, the diagnosis of a particular event may not apply to others.

Yasunaka and Hanawa (2006) examined the relationship between summer temperatures in Japan and large-scale atmospheric fields and showed that the leading mode of surface temperature variability over Japan is related to the strength of the Tibetan high, whereas the second mode is related to the PJ pattern and fluctuations of the Okhotsk high. Such analyses have been conducted to date (e.g., Wakabayashi and Kawamura 2004), but are mostly based on monthly or seasonal mean data. In reality, extreme hot/cold events occur at sub-monthly time scales and require a full investigation of the relationship between Japan’s temperature and large-scale circulation variability using daily data.

In this study, a combined analysis was conducted to examine the relevance of the three major teleconnection patterns in generating anomalously high temperatures during mid-summer (July-

August, hereafter denoted as JA) in Japan over the past six decades. The analysis was conducted using low-pass filtered daily data to identify a direct correspondence between the Japanese heat waves and the background circulation anomaly. We subsequently built a statistical model using the relationship between the three teleconnection indices and temperature over Japan to reconstruct anomalous hot events, which are defined as events accompanying anomalous hot days (defined later). This enabled us to quantitatively estimate the contribution of each teleconnection pattern to Japan's temperature extremes. Such an estimation will be helpful to verify the predictability of anomalous hot events *ex post facto*, as it allows us to determine which patterns we should have focused on to predict a particular anomalous hot event. Furthermore, we examined whether the reconstructed anomalous high-temperature events showed an increasing trend, as seen in the observed data.

The data and methodology are described in section 2. The extraction of the three teleconnection patterns on a daily basis is described in section 3, and their relationship with temperature anomalies over Japan is examined. In section 4, the reconstruction of summer temperature variability over Japan using a statistical model is described, along with the relative contribution of the three patterns to the occurrence of anomalously high temperatures in Japan. Section 5 provides a summary and discussion of the results.

2. Data and methods

2.1. Reanalysis data

We used the JRA-55 atmospheric reanalysis dataset for 1958–2019 (Kobayashi et al. 2015). Daily anomalies were calculated by averaging the 6-hourly data, from which the climatological mean for 1981–2010 was subtracted. After a low-pass filter with a cut-off period of 8 days (tangent-Butterworth recursive filter) was applied to the daily anomaly data, we used the July and August data for the present analysis. In Japan, hot weather conditions normally occur after the end of the Baiu rainy season in mid-July, July and August being the hottest season (Fig. S1), while the summer season is generally considered from June to August in the Northern Hemisphere mid- or high-latitudes. Spatial smoothing was applied to the relative vorticity (ζ) by expanding ζ into a wave space and subsequently suppressing the small-scale wave components (roughly corresponding to a horizontal scale of 8×10^2 km) using a Gaussian filter. For the stream function, we removed a hemispheric average that did not affect the circulation pattern in advance. We also used the fifth generation of the European Centre for Medium-Range Weather Forecasts (ERA5) reanalysis dataset for the same period (Hersbach et al. 2020) and confirmed that the main results of this study are valid for ERA5. For this reason, only results for JRA-55 are shown unless otherwise noted.

2.2. Index for the temperature variability over Japan

Heat waves are conventionally defined using the surface air temperature (SAT) at weather stations. However, the number of stations is limited, and the SAT is influenced by local orography and land surface conditions, such as heat islands in cities. Therefore, we used gridded temperatures at 850 hPa derived from JRA-55 and averaged them over grid cells that cover the land area of Japan, excluding small islands (Fig. S2). This was done to measure the surface temperature variability in Japan (hereafter referred to as T850JP). T850JP well represents the surface temperature variability over Japan, both in terms of the number of extremely (or anomalous) hot days (Figs. 1a and 1b; $r = 0.74$) and the JA mean anomalies (Figs. 1b and 1c; $r = 0.81$). There is a significant positive trend in the anomalous hot days at 850 hPa, indicating that the number of anomalous hot days has increased by 1.06 days per decade at 850 hPa, as with the number of extremely hot days at the surface (0.44 days per decade), although their definition differs from anomalous hot days at 850 hPa. This increasing trend in the number of anomalous days is accompanied by the warming of the JA mean T850JP at a rate of 0.07 K per decade.

2.3. Extracting the dominant modes of circulation variability

To extract the three major teleconnection patterns described in the introduction, we applied an empirical orthogonal function (EOF) analysis separately to the daily low-pass filtered vorticity anomalies at 850 hPa over the subtropical western Pacific (PJ pattern), meridional wind anomalies at 200 hPa over the Asian jet region (CGT pattern), and stream function anomalies at 250 hPa over the Siberian region (Siberian pattern). These domains are shown as thick black line rectangular boxes in Figs. 2–4, and the choice of variables and analysis domains refer to previous studies that extracted the PJ (Kosaka et al. 2013), CGT (Yasui and Watanabe 2010), and Siberian (Arai and Kimoto 2008) patterns. Specifically, the PJ pattern prevails in the lower troposphere, whereas the CGT and Siberian patterns are trapped by the subtropical and polar jets, with cores at approximately 200 and 250 hPa levels, respectively.

2.4. Statistical model

A statistical model to reconstruct the T850JP time series is based on multivariate linear regressions that consider the temporal lag between the predicters and predictands (i.e., T850JP). The predicters are principal components (PCs) associated with the leading EOFs that represent the three teleconnection patterns (Section 3.1). The multivariate regression model assumes a linear relationship between predicters x and predictands $\boldsymbol{y}$, as well as independence among predicters, that is,

$$\boldsymbol{y}(t) = \boldsymbol{\beta} x(t) + \beta_0 + \boldsymbol{\varepsilon}(t) \quad , \qquad (1)$$

where $\boldsymbol{\beta}$ and β_0 are time-invariant vectors and scalers obtained as regression coefficients, which are estimated by minimizing the root-mean-square error, $\sum_i \varepsilon_i^2$.

The evaluation of the model performance was measured by the correlation coefficient (r) between $\boldsymbol{y}(t)$ and $\boldsymbol{\beta x}(t) + \beta_0$, and a determination coefficient, which is equivalent to the square of the correlation coefficient in this case and is therefore denoted as r^2. The determination coefficient is defined as

$$r^2 = 1 - \frac{\sum_i \varepsilon_i^2}{\sum_i y_i^2} \ . \quad (2)$$

Details of the model construction are further described in section 4.1.

3. Dominant teleconnection patterns in relevance to the T850JP variability

3.1. PJ, CGT, and Siberian patterns

Figure 2 shows the two leading EOFs to the 850 hPa vorticity over the subtropical western Pacific (box region). They account for 13.2% and 9.6% of the total variance, respectively, and are statistically separated from other EOFs (North et al. 1982). The first EOF showed a meridional tripole pattern with maxima of vorticity anomalies around the Philippines and Japan (Fig. 2a). The spatial pattern of EOF1 resembled that of the PJ pattern detected by Kosaka et al. (2013; in their Fig. 2A), and the JA mean of the PC was significantly correlated ($r = 0.74$) with a station-based index of the PJ pattern defined by Kubota et al. (2016). EOF1 is related to convection over the Philippine Sea region, or negative anomalies of outgoing longwave radiation over the region (Fig. S3). Its JA mean interannual time series has a weak negative correlation with the Niño 3 index of the previous winter ($r = -0.37$), which is consistent with the literature suggesting that the PJ pattern can be excited by El Niño/La Niña events (Kosaka et al. 2013). The second EOF, which was clearly separated from the first one as mentioned above, has almost the same wavenumber as the first EOF, but is in the orthogonal phase. This mode has a feature similar to that of the first mode in that a wave of a similar wavenumber propagates between the tropical Pacific region and Japan. In fact, EOF2 has a significant correlation with convective activity near the Philippines (Fig. S3), and its JA mean interannual time series is highly correlated with the JA mean South Oscillation Index (SOI; $r = 0.60$). Thus, we refer to the first and second EOFs as the PJ1 and PJ2 patterns in this study, respectively. We regard the associated PC1 and PC2 time series as indices of PJ teleconnections. The PJ2 pattern only shows a weak connection to T850JP as a node of the spatial pattern that lies over Japan (Fig. 2b).

The CGT comprises a zonally migrating wave train without a preferred phase and is therefore defined by two leading EOFs to the 200 hPa meridional wind anomalies (Fig. 3). Both EOFs explained a similar fraction of the total variance (14.4% and 12.4%) and showed a zonal wavy pattern with a phase shift in quadrature along the Asian jet. In both EOFs, the zonal phase is tilted westward with a height around 60° E, indicating a baroclinic structure, while the vertical structure is nearly equivalent to barotropic over Japan (Fig. S4), which is consistent with the results of Terao (1998) and Kosaka et al. (2009). Hereafter, these EOFs are called the CGT1 and 2 patterns, respectively, and their PC time series is considered as an index. The positive phase of the CGT2 pattern was accompanied by an upper-level high in Japan (Fig. 3b).

Two leading EOFs to the 250 hPa stream function anomalies over the Siberian region show distinct patterns (Fig. 4). The first EOF is characterized by a large patch of anomalies over Siberia, where blocking often occurs (Fig. 4a). Notably, the blocking high is clearly identified in a composite map of the 250 hPa geopotential height and the isentropic potential vorticity at 330 K when the corresponding PC shows a negative value below a standard deviation of -2 (Fig. 5a). Conversely, the flow was zonal in the positive phase of the EOF (Fig. 5b). Based on the spatial features of these composite circulations, we refer to the EOF1 to the Siberian pattern, which represents the Siberian blocking in its negative phase.

3.2. Relationship between the three teleconnection patterns and T850JP

Figure 6 shows the composite anomalies of T850JP plotted on an EOF phase space. Notably, the PJ and CGT are represented by both axes of the PCs to the 850 hPa vorticity (Fig. 6a) and 200 hPa meridional wind (Fig. 6b), respectively, and the axis of PC1 to the 250 hPa stream function denotes the Siberian pattern (Fig. 6c). Although the composite T850JP anomalies were not very smooth, they tended to be positive with positive PJ1, CGT2, and Siberian patterns. This strongly suggests that these three patterns are the primary modes of variability that explain T850JP variability.

We conducted an additional analysis from a contrasting perspective. Namely, we investigated whether the above teleconnection patterns prevailed in the circulation anomaly fields when T850JP was anomalously positive. As such, we calculated the lagged regression anomalies of the 850 hPa vorticity, 200 hPa meridional wind, and 250 hPa stream function on the T850JP anomaly (Fig. 7). When circulation anomalies led by three days, the T850JP anomaly, low-level PJ1 pattern, and upper-level CGT2 and Siberian patterns were identified (Fig. 7, top panels). They persisted for at least the subsequent three days (Fig. 7, bottom panels). This lagged relationship between T850JP and the three teleconnections is clearly observed in the regression diagram of the T850JP anomaly on the teleconnection pattern indices (i.e., PC time series; Fig. 8). The peaks of the regression coefficients occur when the PJ1 pattern leads by two days and the CGT2 and Siberian patterns lead by one day.

4. Results of the statistical model

4.1. Construction of the model

Based on the results in the previous section, statistical model (1) is now rewritten more specifically as follows:

$$\mathrm{T850JP}^*(t) = \beta_1 x_1(t-2) + \beta_2 x_2(t-1) + \beta_3 x_3(t-1) + \beta_0 \quad , \qquad (3)$$

where T850JP* is the reconstructed time series of T850JP, x_1, x_2 and x_3 are the PJ1, CGT2, and Siberian pattern indices, respectively. Four model parameters of β are estimated using the multivariate regression for 1958–2019 as $\beta_1 = 0.41 \pm 0.04$ K, $\beta_2 = 0.45 \pm 0.04$ K, $\beta_3 = 0.45 \pm 0.04$ K, and $\beta_0 = 0.10 \pm 0.04$ K, where the range denotes the 95% confidence interval.

The correlation coefficient between T850JP and T850JP* for the entire period of JA from 1958–2019 was $r = 0.57$, which is equivalent to the determination coefficient of $r^2 = 0.32$. This implies that the statistical model could explain approximately 32% of the T850JP variance using the three patterns. This contribution rate is reasonable, given that each pattern explains only 13%–17% of the total variance in the respective field (see Section 5). The regression coefficients in the model, as stated above, show similar values; therefore, the three teleconnection patterns roughly equally contribute to T850JP*.

In addition to the reconstruction of T850JP, the same statistical model can be applied at each grid point to reconstruct the three-dimensional atmospheric anomaly fields associated with the three teleconnection patterns. Namely,

$$\boldsymbol{y}^*(\lambda,\varphi,t) = \boldsymbol{\beta}_1(\lambda,\varphi)x_1(t-\tau_1) + \boldsymbol{\beta}_2(\lambda,\varphi)x_2(t-\tau_2) + \boldsymbol{\beta}_3(\lambda,\varphi)x_3(t-\tau_3) + \boldsymbol{\beta}_{\mathbf{0}}(\lambda,\varphi) \quad , \qquad (4)$$

where $\boldsymbol{y*}$ is a reconstructed anomaly field as a function of longitude (λ), latitude (φ), and time (850 hPa temperature or 500 hPa geopotential height). τ_i $(i = 1, 2, 3)$ was defined at each grid such that the absolute value of the regression coefficient of x_i on $\boldsymbol{y}^*$ becomes the largest at $t = \tau_i$ between -5 and +5 days.

The determination coefficient also displays a spatial structure, whose pattern reveals the extent to which the anomaly at each grid point can be explained by the sum of the three teleconnection patterns (Fig. 9). A relatively high value is observed over Siberia, the Philippines, Japan, and central Eurasia, where the three patterns dominate. The pattern of the determination coefficient also shows a high value in northern Japan. In southern Japan, a node of the PJ1 pattern lies and anomalous horizontal advection accompanied by the Siberian pattern does not reach it. Thus, the temperature variability in southern Japan cannot be satisfactorily explained by the combination of the three teleconnections.

4.2. Case studies for extreme hot events

There have been several heat waves in Japan over the last decade, and the statistical model can only capture some of them. The T850JP anomaly time series for the 2018 and 2013 summers are shown in Figs. 10 and 11, respectively, as examples of the success and failure of reproducing past heat waves.

In 2018, T850JP recorded a high value in the middle of July until the end of the month, and subsequently returned to normal in early August (black curve in Fig. 10a). This time evolution is reconstructed by T850JP* even though its magnitude is underestimated (red curve in Fig 10a). Anomalies in the 500 hPa geopotential height and 850 hPa temperature average during the heat wave (from July 12 to 31) were also similar between JRA-55 and the statistical model (Figs. 10b and 10c). This similarity suggests that the extreme hot event in July 2018 can be primarily explained by these three patterns, with positive PJ1 and Siberian patterns (i.e., zonal flow) having roughly the same impact on T850JP. Conversely, the statistical model failed to reconstruct the T850JP anomaly time series in 2013 when another heat wave occurred during mid-August (Fig. 11). The three teleconnection patterns are suggested to have a minor influence on this event. This result is consistent with Imada et al. (2014), who suggested that there are anthropogenic causes behind the heat wave in 2013, with higher sea surface temperature (SST) around Japan compared to non-warming experiments, and La Niña-like SST conditions strengthening the Pacific High.

We examined other hot summers in 1961, 1978, 1994, and 2010 according to the past *Moushobi* record (Fig. 1a). We found that our statistical model works well for most of the summers in reproducing the high-temperature events in terms of its intensity and phase, strengthening the validity of the model (Fig. S5). The same model can be applied to cold summers, as shown in Fig. S6, which confirms that our model is valid for cold summers, showing a determination coefficient significantly higher than 0.32, which is calculated throughout the entire period. The skill of our statistical model can be further visualized by plotting the determination coefficient between T850JP and T850JP* against the JA mean T850JP for each year (Fig. S7). Note that the determination coefficient calculated based on only a portion of the total time series is not necessarily non-negative (r^2 is just a notation; see Eq. (2)). A negative determination coefficient means that the model is less accurate than if we were expecting T850JP to be zero all the time. Such inaccuracies occurred in 10 of the 62 years analyzed. For anomalous hot/cold summers, when the JA mean T850JP anomalies are above or below +1 K/-1 K, determination coefficients are $r^2 = 0.50 \pm 0.12, 0.54 \pm 0.11$, respectively (the range represents one standard deviation), showing that our statistical model is valid for anomalous temperature events. Note that for a year in which the absolute value of JA mean T850JP shows a relatively small figure, the determination coefficient is below zero, which means that our model is less accurate than expecting T850JP to be zero every day. This may be because of the fact that the denominator of the second term on the right-hand side of equation (2) becomes smaller because the variance of T850JP is smaller.

4.3. Interannual variability and warming trends

Given the close correspondence between the occurrence frequency of anomalous hot days and the mean temperature anomaly (Figs. 1b and 1c), it is vital to use the statistical model to examine the contribution of the three teleconnection patterns to the interannual fluctuation of the JA mean T850JP (Fig. 12b). The T850JP variability at this time scale can be reproduced well by T850JP*, as represented by their significant correlation ($r = 0.56$).

Both T850JP and T850JP* show increasing trends (0.07 and 0.04 K per decade, respectively) statistically significant with 95% confidence level; however, the latter was underestimated compared to the former. The time series of the number of anomalous hot days based on the daily T850JP (Fig. 1b) is also reproduced by T850JP* to a certain extent, and both time series show similar increasing trends (1.06 and 0.97 days per decade; Fig. 12a) as with the statistical model based on the ERA5 reanalysis data (Fig. S8). This warming trend is subtle compared to the daily fluctuations, but histograms of T850JP and T850JP* for the first (1958–1988) and second (1989–2019) halves are discernibly different (Fig. S9).

The relative contributions of the three teleconnections to the interannual variability and long-term trends in T850JP can be quantified using Eq. (3), to which all but one regression coefficient is set to zero (Fig. 13). When the PJ1 pattern is a single predictor, T850JP* shows the maximum correlation with T850JP, both in terms of the number of anomalous hot days ($r = 0.38$) and the JA mean anomalies ($r = 0.55$). Note that the correlation coefficient between the PJ1 pattern and JA mean T850JP is almost the same as that obtained by the statistical model, as opposed to the results obtained in Section 4.1. This difference may be attributed to a longer timescale of the PJ1 pattern compared with the other two patterns, as the PJ1 pattern seems to have a memory from the previous winter Niño 3 index. Meanwhile, other PCs are not well correlated with the Niño-related index regardless of the time lag.

In contrast, the long-term trends in these variables can be better reproduced when the CGT2 pattern is a single predictor (0.02 K per decade and 1.06 days per decade, both statistically significant at the 95% confidence level), as with the model based on ERA5 (Fig. S10). Notably, a comparison of the histograms of the CGT2 index for 1958–1988 and 1989–2019 shows that the positive CGT2 pattern tends to appear more frequently in recent decades (Fig. S11), which increased the number of anomalous hot days in Japan. The correlation between the JA mean CGT2 index and the JA mean temperature at 850 hPa over the Northern Hemisphere is also significant ($r = 0.34$). The JA mean CGT1 index also showed a long-term decreasing trend, similar to the CGT2 index, although the sign is opposite. The sign of the linear trend is not critical as it depends on the pattern of the positive phases in the EOF analysis. As in the CGT1 index, the JA mean CGT2 index is correlated with the JA mean temperature at 850 hPa over the Northern Hemisphere ($r = -0.32$). These analyses imply that the long-term trends in the CGT indices may be a consequence of ongoing global warming, but further research is required to clarify the effects of global warming on the occurrence of the CGT pattern.

5. Summary and discussion

This study aimed to quantify the influence of major teleconnection patterns on anomalous hot events during mid-summer (July-August) in Japan using JRA-55 reanalysis data. Three modes of large-scale circulation variability are extracted using the EOF analysis: PJ, CGT, and Siberian patterns, which are all dominant in the low-pass filtered daily anomaly fields. The PJ teleconnection consists of two EOF patterns representing a different meridional phase. Both PJ1 and PJ2 indices are highly correlated with the Niño 3 index and SOI, indicating an influence from El Niño-Southern Oscillation, while other teleconnection patterns are not correlated with the Niño-related indices. The Siberian pattern includes blocking in its negative phase, and the zonal phase corresponding to the positive phase accompanies the positive low-level temperature anomaly around Japan.

We demonstrated that T850JP showed a large positive anomaly one or two days after the positive peak of the three teleconnection patterns. The three patterns prevail in composite anomaly maps in reference to the large positive T850JP anomaly, confirming their close relationship. Based on these findings, we reconstructed T850JP from three teleconnection indices using a statistical method. We found that they together explained about 32% of the total variance of daily T850JP anomalies, with a similar degree of contribution on a sub-weekly timescale. The contribution of the three teleconnection patterns to T850JP is not constant during the analysis period and shows $r^2 = 0.50 \pm 0.12$ and

0.54 ± 0.11 for anomalous hot and cold summer, respectively. We reconstructed T850 and Z500 for each grid from the three indices using the same statistical method and showed that the three patterns have a greater impact in northern Japan than in southern Japan.

The fractional variance of T850JP explained by the combination of the three teleconnection patterns is apparently not high. However, given that each teleconnection explains only 13–17% of the total variance in the respective circulation fields (i.e., variables and domain for the EOF analysis), the total fractional contribution will not be considerably larger. Nevertheless, it is possible that the assumptions for the statistical model underestimated their contribution. First, the linearity assumed for the relationship between each pattern and T850JP might not be the case when they have large amplitudes (Fig. S12). Second, independence among teleconnection patterns might not always be valid (Table S1). Extreme weather events sometimes occur due to a sequence of phenomena and/or the co-occurrence of multiple teleconnections. Hirota and Takahashi (2012) suggested that the PJ and Siberian patterns are coupled through convection anomalies around Japan. Takemura and Mukougawa (2020) also showed that the PJ pattern can be excited when a quasi-stationary Rossby wave associated with the CGT pattern propagates and breaks at the eastern edge. An extension of the statistical model that incorporates the co-dependence among teleconnection patterns may better reproduce anomalous hot events in terms of T850JP.

Notably, the statistical model could reproduce the long-term warming trend in T850JP without the explicit inclusion of global warming as a predictor. The influence of the CGT pattern is thought to be the dominant source of this warming trend. Detecting a robust response of regional atmospheric circulation to global warming is still challenging (Shepherd 2014); therefore, the impact of global warming on the occurrence of the CGT pattern would be a vital aspect in future studies.

Supplement

Supplement contains 12 figures and a table, which show the results of additional analyses including the analyses based on ERA5.

Acknowledgments

The authors thank the two anonymous reviewers for their constructive comments. This work was supported by Grant-in-Aid 26247079 and the Integrated Research Program for Advancing Climate Models (JPMXD0717935457) from the Ministry of Education, Culture, Sports, Science and Technology (MEXT), Japan. We also thank the Copernicus Climate Change Service (C3S) for providing the ERA5 dataset which is available at https://cds.climate.copernicus.eu/cdsapp#!/home.

References

Arai, M., and M. Kimoto, 2008: Simulated interannual variation in summertime atmospheric circulation associated with the East Asian monsoon. *Clim. Dyn.*, **31**, 435-447; Corrigendum. *Clim. Dyn.*, **51**, 1605-1608.

Ding, Q., and B. Wang, 2005: Circumglobal teleconnection in the Northern Hemisphere summer. *J. Climate*, **18**, 3483-3505.

Enomoto, T., B. J. Hoskins, B. J., and Y. Matsuda, 2003: The formation mechanism of the Bonin high in August. *Quart. J. Roy. Meteor. Soc.*, **129**, 157-178.

Fujibe, F., 2013: Long-term variations in heat mortality and summer temperature in Japan. *Tenki*, **60**, 371-381 (in Japanese).

Fujibe, F., J. Matsumoto, and H. Suzuki, 2018a: Regional features of the relationship between daily heat-stroke mortality and temperature in different climate zones in Japan. *SOLA*, **14**, 144-147.

Fujibe, F., J. Matsumoto, and H. Suzuki, 2018b: Spatial and temporal features of heat stroke mortality in Japan and their relation to temperature variations, 1999-2014. *Geogr. Rev. Japan*, **91**, 17-27.

Guan, Z., and T. Yamagata, 2003: The unusual summer of 1994 in East Asia: IOD teleconnections. *Geophys. Res. Lett.*, **30**, 1544.

Hersbach, H., B. Bell, P. Berrisford, S. Hirahara, A. Horányi, J. Muñoz-Sabater, J. Nicolas, C. Peubey, R. Radu, D. Schepers, A. Simmons, C. Soci, S. Abdalla, X. Abellan, G. Balsamo, P. Bechtold, G. Biavati, J. Bidlot, M. Bonavita, G. D. Chiara, P. Dahlgren, D. Dee, M. Diamantakis, R. Dragani, J. Flemming, R. Forbes, M. Fuentes, A. Geer, L. Haimberger, S. Healy, R. J. Hogan, E. Hólm, M. Janisková, S. Keeley, P. Laloyaux, P. Lopez, C. Lupu, G. Radnoti, P. de Rosnay, I. Rozum, F. Vamborg, S. Villaume, and J.-N. Thépaut, 2020: The ERA5 global reanalysis. *Quart. J. Roy. Meteor. Soc.*, **146**, 1999–2049.

Hirota, N., and M. Takahashi, 2012: A tripolar pattern as an internal mode of the East Asian summer monsoon. *Clim. Dyn.*, **39**, 2219-2238.

Hoskins, B. J., and T. Ambrizzi, 1993: Rossby wave propagation on a realistic longitudinally varying flow. *J. Atmos. Sci.*, **50**, 1661-1671.

Imada, Y., H. Shiogama, M. Watanabe, M. Mori, M. Ishii, and M. Kimoto, 2014: The contribution of anthropogenic forcing to the Japanese heat waves of 2013, in "Explaining Extreme Events of 2013 from a Climate Perspective", *Bull. Amer. Meteor. Soc*., **95**(9), S52-S54.

Imada, Y., M. Watanabe, H. Kawase, H. Shiogama, and M. Arai, 2019: The July 2018 high temperature event in Japan could not have happened without human-induced global warming. *SOLA*, **15A**, 8-12.

Japan Meteorological Agency, 2018: Press release on the July heavy rain event and subsequent hot extremes in 2018 (in Japanese), https://www.jma.go.jp/jma/press/1808/10c/h30goukouon20180810.html

Kobayashi, S., Y. Ota, Y. Harada, A. Ebita, M. Moriya, H. Onoda, K. Onogi, H. Kamahori, C. Kobayashi, H. Endo, K. Miyaoka, K. Takahashi, 2015: The JRA-55 reanalysis: General specifications and basic characteristics. *J. Meteor. Soc. Japan.*, **93**, 5-48.

Kosaka, Y., and H. Nakamura, 2008: A comparative study on the dynamics of the Pacific-Japan (PJ) teleconnection pattern based on reanalysis datasets. *SOLA*, **4**, 9-12.

Kosaka, Y., H. Nakamura, M. Watanabe, and M. Kimoto, 2009: Analysis on the dynamics of a wavelike teleconnection pattern along the summertime Asian jet based on a reanalysis dataset and climate model simulations. *J. Meteor Soc. Japan*. **87**, 561-580.

Kosaka, Y., S. P. Xie, N. C. Lau, and G. A. Vecchi, 2013: Origin of seasonal predictability for summer climate over the Northwestern Pacific. *Proc. Nat. Acad. Sci.*, **110**, 7574-7579.

Kubota, H., Y. Kosaka, and S. P. Xie, 2016: A 117-year long index of the Pacific-Japan pattern with application to interdecadal variability. *Int. J. Climatol.*, **36**, 1575-1589.

Nakai, S., T. Itoh, and T. Morimoto, 1999: Deaths from heat-stroke in Japan: 1968–1994. *Int. J. Biometeor.,* **43**, 124-127.

Nakamura, H., and T. Fukamachi, 2004: Evolution and dynamics of summertime blocking over the Far East and the associated surface Okhotsk high. *Quart. J. Roy. Met. Soc.*, **130**, 1213-1233.

Nitta, T., 1987: Convective activities in the tropical western Pacific and their impact on the Northern Hemisphere summer circulation. *J. Meteor. Soc. Japan*, **65**, 373-390.

North, G. R., T. L. Bell, R. F. Cahalan, and F. J. Moeng, 1982: Sampling errors in the estimation of empirical orthogonal functions. *Mon. Wea. Rev.*, **110**, 699-706.

Park, Y. J., and J. B. Ahn, 2014: Characteristics of atmospheric circulation over East Asia associated with summer blocking. *J. Geophys. Res.*, **119**, 726-738.

Park, C. K., and S. D. Schubert, 1997: On the nature of the 1994 East Asian summer drought. *J. Climate*, **10**, 1056-1070.

Shepherd, T., 2014: Atmospheric circulation as a source of uncertainty in climate change projections.

Nat. Geosci., **7**, 703–708.

Takemura, K. and H. Mukougawa, 2020: Dynamical relationship between quasi-stationary Rossby wave propagation along the Asian jet and Pacific-Japan pattern in boreal summer. *J. Meteor. Soc. Japan*, **98**, 169-187.

Terao, T. 1998: Barotropic disturbances on intraseasonal time scales observed in the midlatitudes over the Eurasian continent during the northern summer. *J. Meteor. Soc. Japan*, **76**, 419-436.

Wakabayashi, S., and R. Kawamura, 2004: Extraction of major teleconnection patterns possibly associated with the anomalous summer climate in Japan. *J. Meteor. Soc. Japan*, **82**, 1577-1588.

Yasui, S., and M. Watanabe, 2010: Forcing processes of the summertime circumglobal teleconnection pattern in a dry AGCM. *J. Climate*, **23**, 2093-2114.

Yasunaka, S., and K. Hanawa, 2006: Interannual summer temperature variations over Japan and their relation to large-scale atmospheric circulation field. *J. Meteor. Soc. Japan*, **84**, 641-652.

Yeo, S. R., S. W. Yeh, and W. S. Lee, 2019: Two types of heat wave in Korea associated with atmospheric circulation pattern. *J. Geophys. Res.*, **124**, 7498-7511.

List of Figures

Figure 1 Observed time series of (a) the number of days when daily maximum temperature exceeds 35 °C (derived from the Japan Meteorological Agency). The number of extremely hot days per station for the 13 sample stations is shown. (b) the number of days when daily T850JP anomaly exceeds one standard deviation, and (c) the July-August (JA) mean T850JP anomaly. Dashed lines denote their linear trends from 1958–2019 (the value indicated in the panel), which are all statistically significant at the 95% level. In (a), the number of days was an average of 13 weather stations having long records (Abashiri, Nemuro, Suttsu, Yamagata, Ishinomaki, Fushiki, Choshi, Sakai, Hamada, Hikone, Tadotsu, Naze, Ishigakijima Island) selected with a criterion that they are least affected by urbanization. Their linear trends for the entire period are shown in the panel.

Figure 2 (a) First and (b) second leading EOFs to the daily low-pass filtered vorticity anomalies at 850 hPa from 1958–2019. The black box denotes the EOF domain, and values are regression coefficients on the corresponding PC time series (contour interval is $2 \times 10^{-6}\ \mathrm{s}^{-1}$ per one standard deviation). The fractional contribution of the respective EOF is shown at the top right. The dark (light) shading indicates the anomalies that are statistically significant at the 99% (95%) level. Red (blue) shading represents positive (negative) values, and solid (dashed) lines indicate non-negative (negative) values.

Figure 3 As in Fig. 2, but for the meridional wind velocity at 200 hPa **(**contour interval is $2\ \mathrm{m\ s}^{-1}$ per one standard deviation**)**.

Figure 4 As in Fig. 2, but for the stream function at 250 hPa (contour interval is $2 \times 10^6\ \mathrm{m}^2\ \mathrm{s}^{-1}$ per one standard deviation).

Figure 5 Composite maps of the geopotential height at 250 hPa (contour interval is 100 m) and the potential vorticity at 330 K (shading) for (a) negative and (b) positive phases of the Siberian pattern, defined by the index below -2 and above +2, respectively. Notably, the values presented are raw fields but not anomalies.

Figure 6 Composite anomalies of the daily low-pass filtered T850JP on a phase space between PC1 and PC2 of (a) 850 hPa vorticity, (b) 200 hPa meridional wind velocity, and (c) 250 hPa stream function. The EOF patterns associated with the PCs are shown in Figs. 2–4.

Figure 7 Anomalies regressed on the daily low-pass filtered T850JP at (top) -3 days and (bottom) 0 day, of 850 hPa vorticity, 200 hPa meridional wind velocity, and 250 hPa stream function (from left to right). The negative lag denotes anomalies preceding T850JP. Other conventions follow Fig. 2.

Figure 8 Lagged regression coefficients of the daily low-pass filtered T850JP anomalies on PJ1, CGT2, and Siberian pattern indices. The negative lag denotes each index preceding T850JP.

Figure 9 Horizontal distribution of the determination coefficient in the statistical model for (a) 850 hPa temperature and (b) 500 hPa geopotential height.

Figure 10 (a) Time series of daily low-pass filtered T850JP anomalies in 2018 summer: JRA-55 (thick black line) and its reconstruction using a statistical model (thick red line). Thin lines denote contributions from PJ1 (red), CGT2 (blue), and Siberian (green) patterns. The value shown in the upper right denotes the determination coefficient between T850JP and T850JP*. (b)-(c) 500 hPa geopotential height anomalies (contour interval is 50 m) and 850 hPa temperature anomalies (shading) averaged from July 12 to 31, 2018 (gray shaded period in (a)), in JRA-55 and the statistical model.

Figure 11 As in Fig. 10, but for 2013 summer. Gray shaded period in (a) is from August 7 to 18, 2013.

Figure 12 Time series of (a) the number of days when the daily T850JP anomaly exceeds one standard deviation and (b) July-August (JA) mean T850JP anomaly, both obtained from the statistical model (red line and bars) imposed on the observed time series shown in Fig. 1 (black line and bars). Dashed lines denote their trends from 1958–2019, which are all statistically significant at the 95% level. The correlation coefficients between the model and observation are shown in the panel.

Figure 13 As in Fig. 12, but for the model T850JP anomalies reconstructed using only the PJ1 (left), CGT2 (middle), and Siberian (right) patterns, respectively. Linear trends for the reconstruction using the CGT2 pattern are statistically significant at the 95% level.

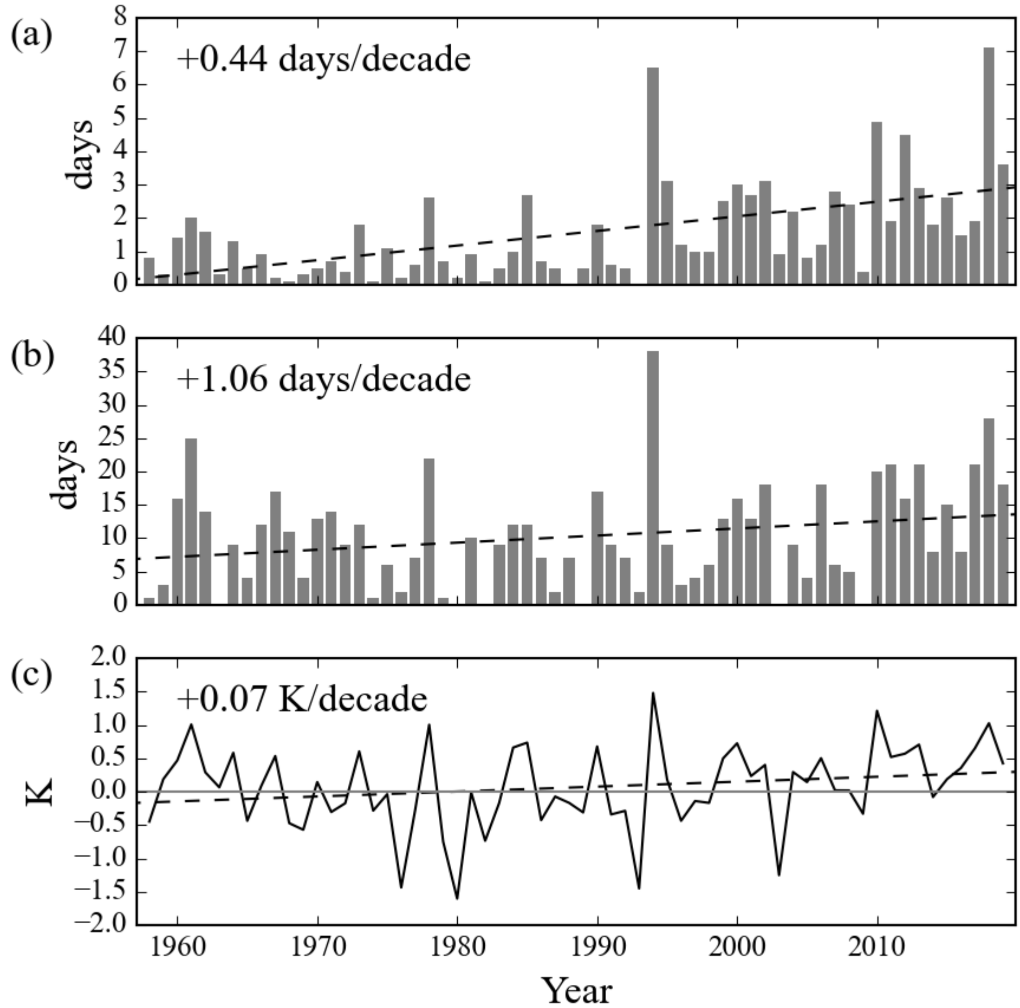

Figure 1 Observed time series of (a) the number of days when daily maximum temperature exceeds 35 °C (derived from the Japan Meteorological Agency). The number of extremely hot days per station for the 13 sample stations is shown. (b) the number of days when daily T850JP anomaly exceeds one standard deviation, and (c) the July-August (JA) mean T850JP anomaly. Dashed lines denote their linear trends from 1958–2019 (the value indicated in the panel), which are all statistically significant at the 95% level. In (a), the number of days was an average of 13 weather stations having long records (Abashiri, Nemuro, Suttsu, Yamagata, Ishinomaki, Fushiki, Choshi, Sakai, Hamada, Hikone, Tadotsu,

Naze, Ishigakijima Island) selected with a criterion that they are least affected by urbanization. Their linear trends for the entire period are shown in the panel.

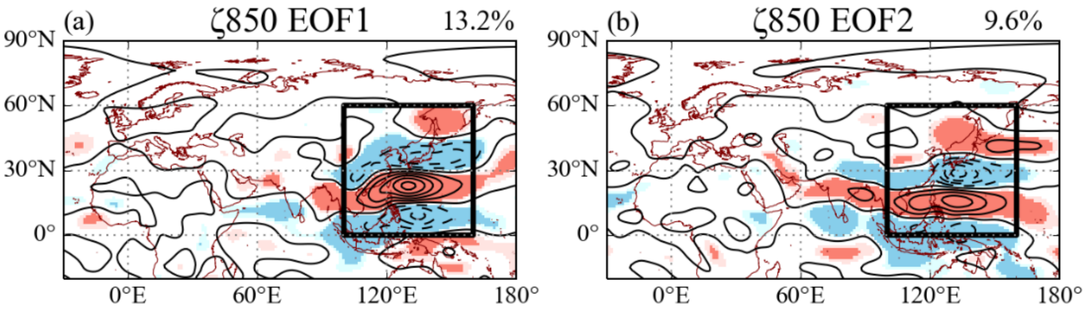

Figure 2 (a) First and (b) second leading EOFs to the daily low-pass filtered vorticity anomalies at 850 hPa from 1958–2019. The black box denotes the EOF domain, and values are regression coefficients on the corresponding PC time series (contour interval is $2 \times 10^{-6}\ \mathrm{s}^{-1}$ per one standard deviation). The fractional contribution of the respective EOF is shown at the top right. The dark (light) shading indicates the anomalies that are statistically significant at the 99% (95%) level. Red (blue) shading represents positive (negative) values, and solid (dashed) lines indicate non-negative (negative) values.

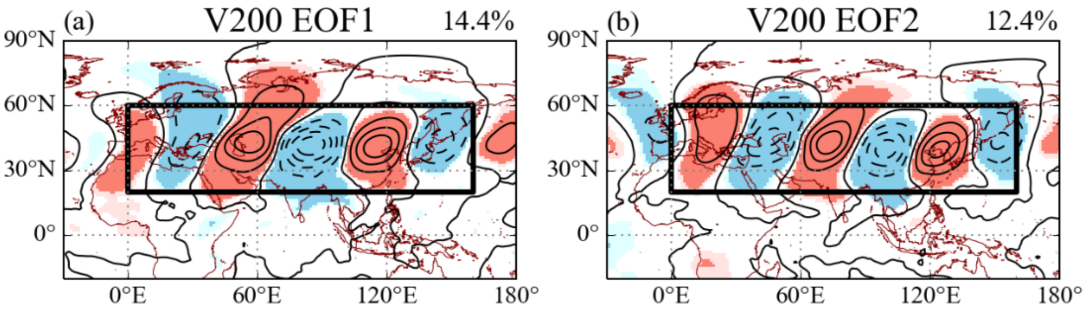

Figure 3 As in Fig. 2, but for the meridional wind velocity at 200 hPa **(**contour interval is 2 m s^{-1} per one standard deviation**)**.

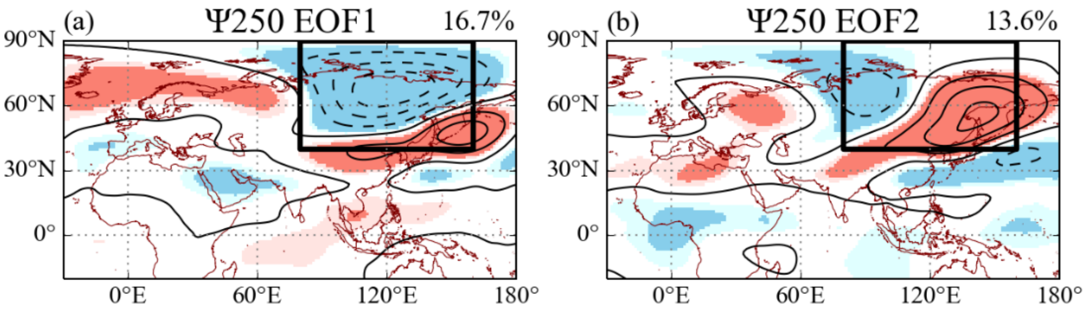

Figure 4 As in Fig. 2, but for the stream function at 250 hPa (contour interval is $2 \times 10^6\ \mathrm{m}^2\ \mathrm{s}^{-1}$ per one standard deviation).

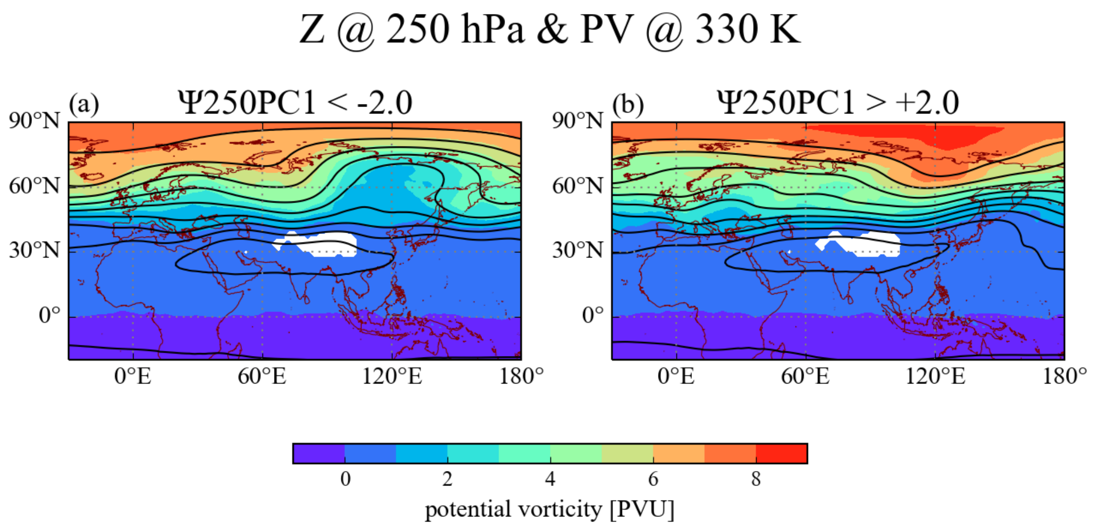

Figure 5 Composite maps of the geopotential height at 250 hPa (contour interval is 100 m) and the potential vorticity at 330 K (shading) for (a) negative and (b) positive phases of the Siberian pattern, defined by the index below -2 and above +2, respectively. Notably, the values presented are raw fields but not anomalies.

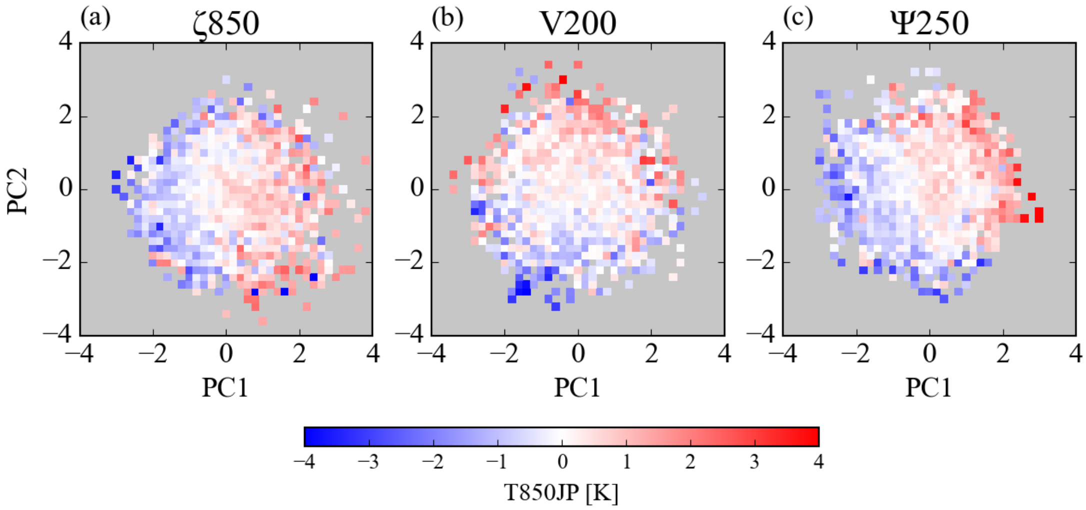

Figure 6 Composite anomalies of the daily low-pass filtered T850JP on a phase space between PC1 and PC2 of (a) 850 hPa vorticity, (b) 200 hPa meridional wind velocity, and (c) 250 hPa stream function. The EOF patterns associated with the PCs are shown in Figs. 2–4.

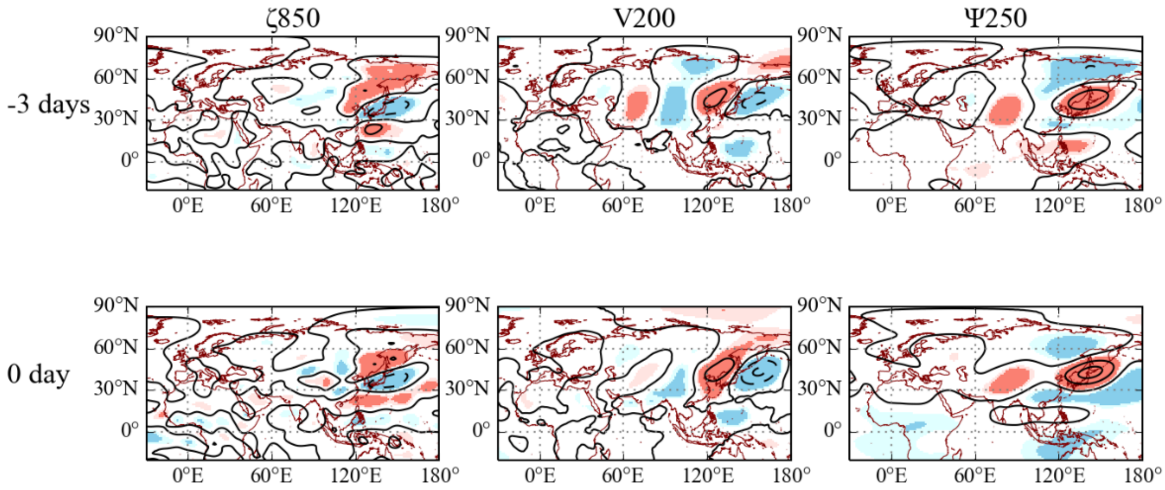

Figure 7 Anomalies regressed on the daily low-pass filtered T850JP at (top) -3 days and (bottom) 0 day, of 850 hPa vorticity, 200 hPa meridional wind velocity, and 250 hPa stream function (from left to right). The negative lag denotes anomalies preceding T850JP. Other conventions follow Fig. 2.

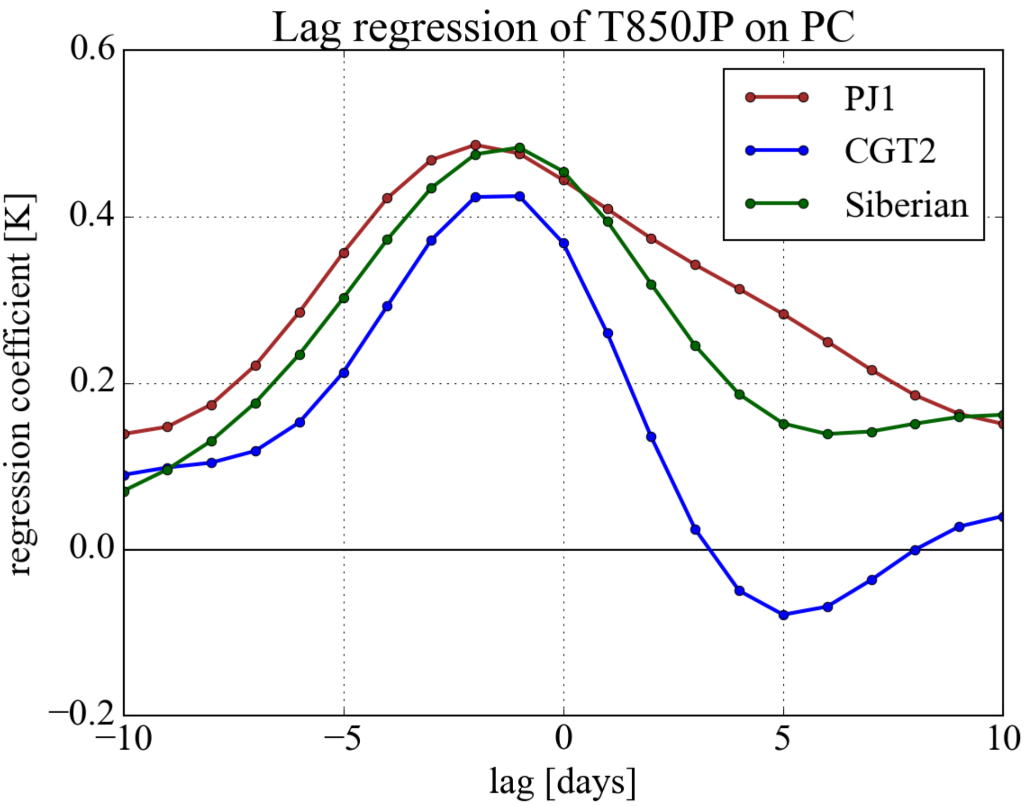

Figure 8 Lagged regression coefficients of the daily low-pass filtered T850JP anomalies on PJ1, CGT2, and Siberian pattern indices. The negative lag denotes each index preceding T850JP.

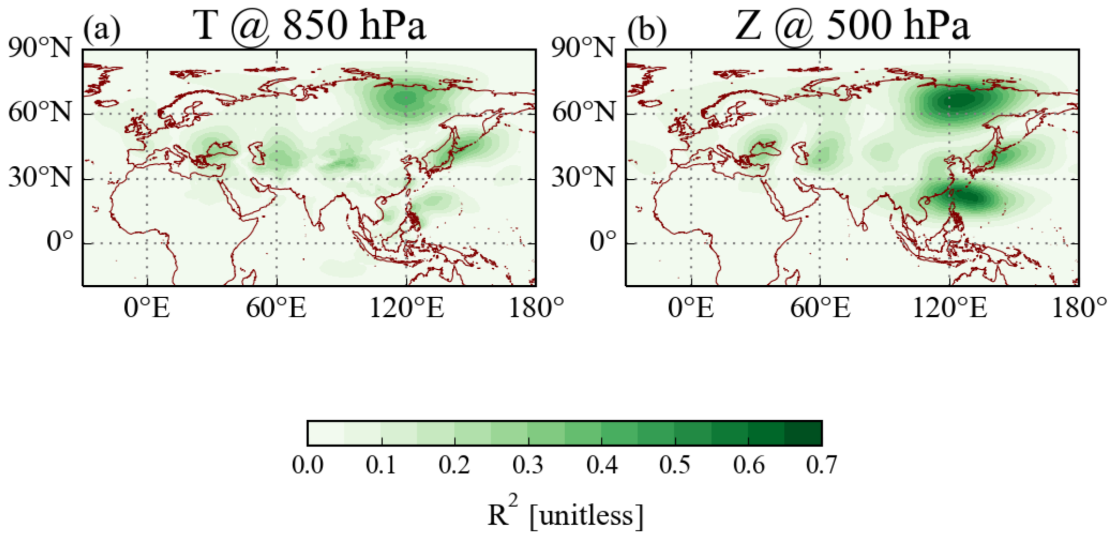

Figure 9 Horizontal distribution of the determination coefficient in the statistical model for (a) 850 hPa temperature and (b) 500 hPa geopotential height.

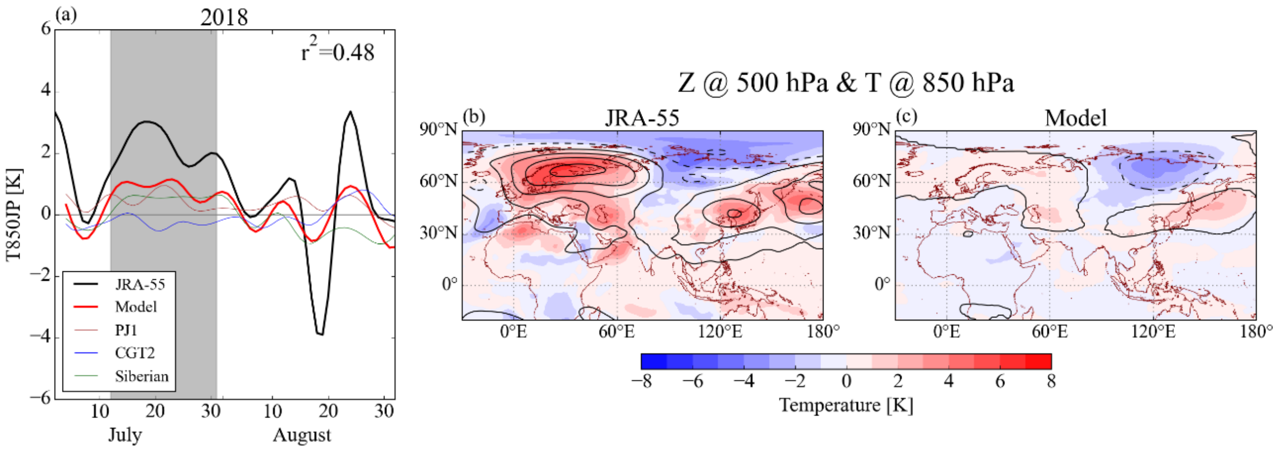

Figure 10 (a) Time series of daily low-pass filtered T850JP anomalies in 2018 summer: JRA-55 (thick black line) and its reconstruction using a statistical model (T850JP*, thick red line). Thin lines denote contributions from PJ1 (red), CGT2 (blue), and Siberian (green) patterns. The value shown in the upper right denotes the determination coefficient between T850JP and T850JP*. (b)-(c) 500 hPa geopotential height anomalies (contour interval is 50 m) and 850 hPa temperature anomalies (shading) averaged from July 12 to 31, 2018 (gray shaded period in (a)), in JRA-55 and the statistical model.

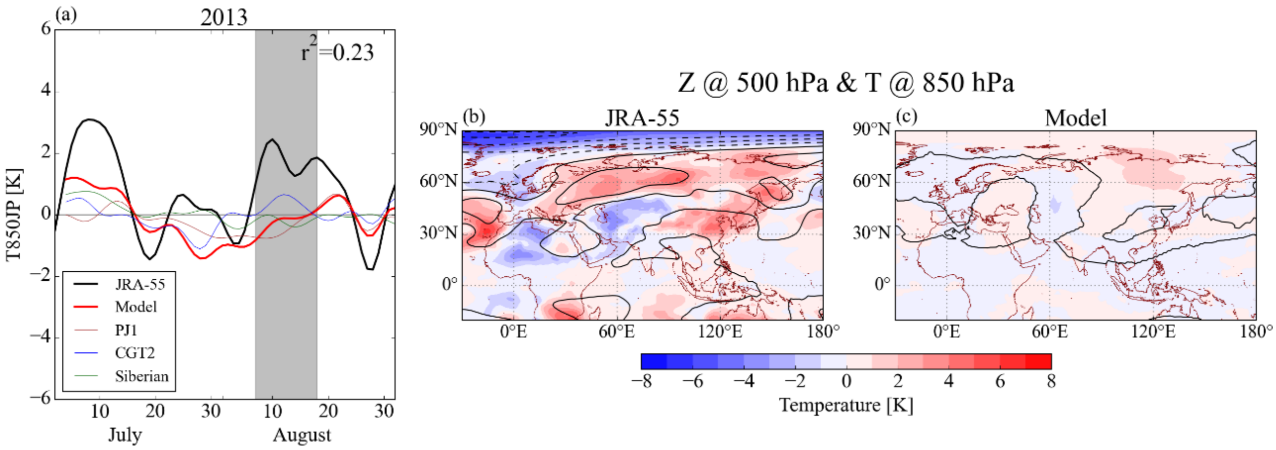

601 **Figure 11** As in Fig. 10, but for 2013 summer. Gray shaded period in (a) is from August 7 to 18, 2013.

602

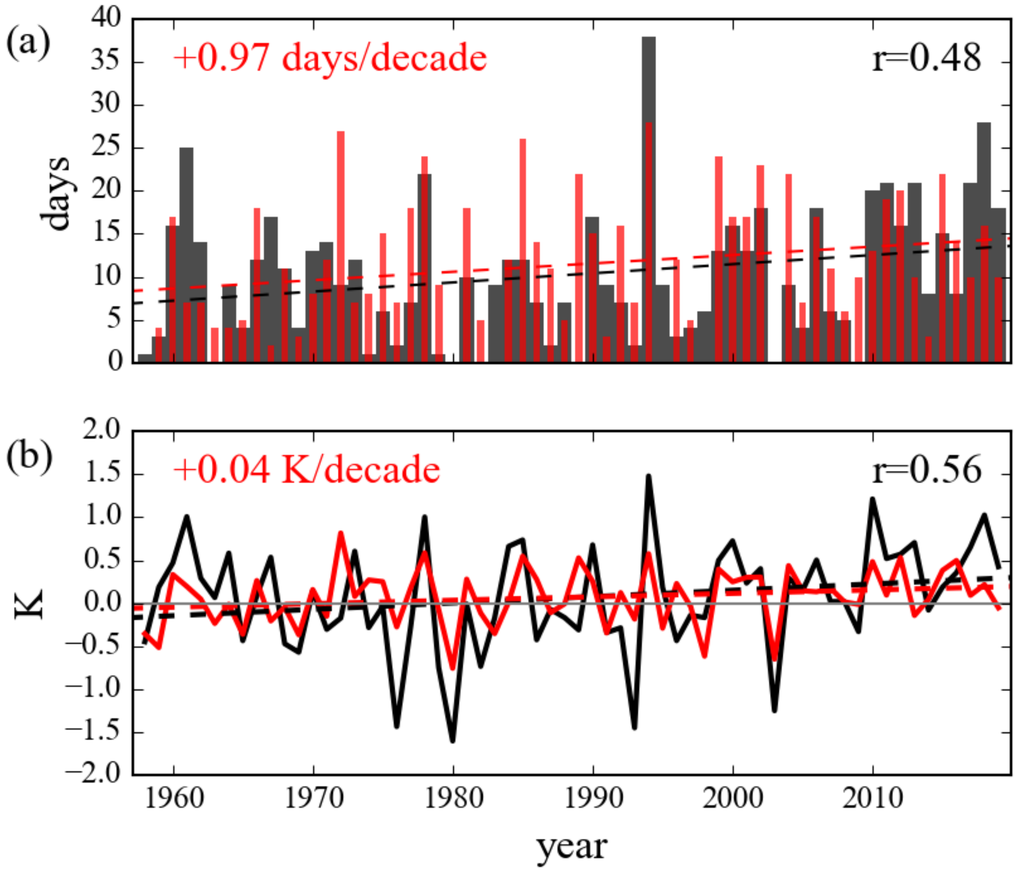

Figure 12 Time series of (a) the number of days when the daily T850JP anomaly exceeds one standard deviation and (b) July-August (JA) mean T850JP anomaly, both obtained from the statistical model (red line and bars) imposed on the observed time series shown in Fig. 1 (black line and bars). Dashed lines denote their trends from 1958–2019, which are all statistically significant at the 95% level. The correlation coefficients between the model and observation are shown in the panel.

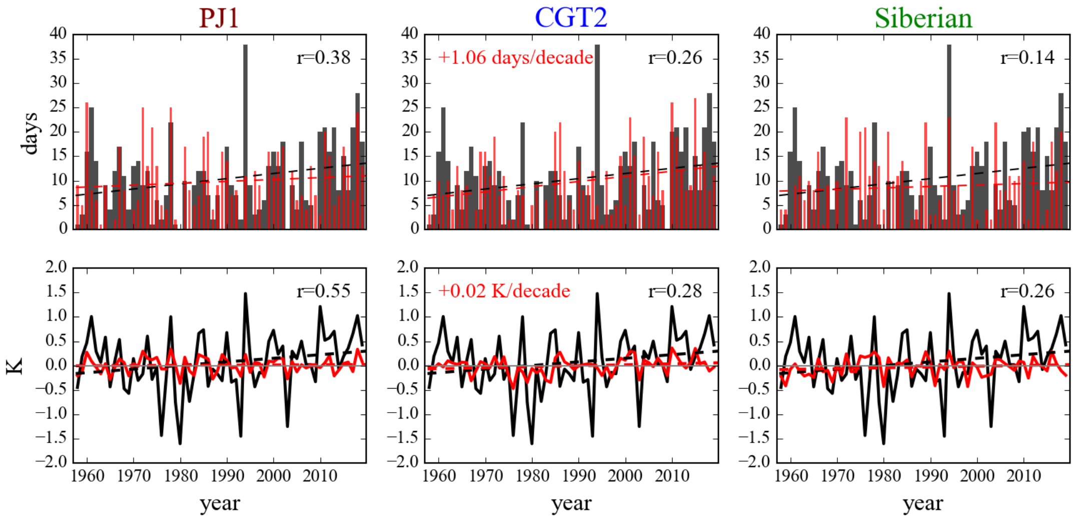

Figure 13 As in Fig. 12, but for the model T850JP anomalies reconstructed using only the PJ1 (left), CGT2 (middle), and Siberian (right) patterns, respectively. Linear trends for the reconstruction using the CGT2 pattern are statistically significant at the 95% level.